Full length article

The role of dopant charge state on defect chemistry and grain growth of doped UO$_2$

M.W.D. Cooper[*], C.R. Stanek, D.A. Andersson

Materials Science and Technology Division, Los Alamos National Laboratory P.O. Box 1663, Los Alamos, NM 87545, USA

ABSTRACT

Additives are widely used to control the microstructure of materials via their effect on defect chemistry during sintering. As the primary nuclear fuel, the properties of UO$_2$ are crucial for safe and efficient reactor operation. UO$_2$ has been manipulated by fuel vendors through doping to enhance grain size to provide improved fission gas retention and plasticity. In this work the common phenomenon that governs the effect of Mg, Ti, V, Cr, Mn, and Fe doping of UO$_2$ for enhanced grain growth is revealed, elucidating experimental observations. A combined density functional theory and empirical potential description of defect free energy is used to calculate the doped UO$_2$ defect concentrations as a function of temperature. At high (sintering) temperatures all dopants studied transition to a positively charged interstitial defect. Furthermore, a number of dopants (Ti, V, Cr, and Mn) do so in sufficiently high concentrations to greatly increase the negatively charged uranium vacancy concentration. High uranium vacancy concentrations can enhance grain growth and fission gas diffusion. Mg and Fe also enhance uranium vacancy concentrations but to a lesser extent, while Al has no impact. The enhanced uranium vacancy concentrations, associated with solution of dopants interstitially, is proposed as the mechanism responsible for the enlarged grains seen experimentally in (Ti/V/Cr/Mg)-doped systems. Mn- and V-doped UO$_2$ have been predicted to have higher uranium vacancy concentrations than the more widely used Cr-doped UO$_2$, leading to higher grain growth and fission gas diffusivity.

© 2018 Acta Materialia Inc. Published by Elsevier Ltd. All rights reserved.

1. Introduction

UO$_2$ is the most widely used nuclear fuel due to its chemical stability, high melting point and radiation tolerance. The release of fission gas (Xe and Kr) creates technical issues during reactor operation. Fission gas release reduces the thermal conductivity of the fuel-cladding gap and increases the fuel rod pressure, which can lead to rod failure. Some incremental fuel concepts use a dopant during pellet sintering to promote grain growth. The aim is to increase the distance travelled (and time taken) during the rate limiting intra-granular diffusion step before rapid fission gas release from the grain boundaries. Cr [1—8], Nb [9—11], Mg [11—13], Ti [11,14], and V [15] additives have all been identified as UO$_2$ grain enlargers. An additional benefit of enlarged grains is increased plasticity and thermal creep, which reduces strain between the pellet and the metal cladding [16—18].

Generally grain growth can be expressed as:

$$\overline{G}^n - \overline{G}_0^n = t \cdot k_0 \exp\left(\frac{-Q}{k_B T}\right) \qquad (1)$$

where $\overline{G}_0$ and $\overline{G}$ are the average grain size before and after annealing, respectively. T is the temperature, t is the annealing time, and k_B is the Boltzmann constant. n is a mechanism dependent parameter and various values have been suggested depending on interactions between pores and grain boundaries [19—25]. The activation energy, Q, and pre-exponential, k_0, are constants for the rate of the mechanism that governs grain growth. For ideal grain growth the dominant mechanism is bulk diffusion and $n = 2$.

Cr-doped UO$_2$, in particular, is frequently studied. Liquid phase sintering due to the CrO eutectic has been identified in the literature as the primary mechanism for enhanced grain growth [1—6]. However, Bourgeois et al. [1] measured an increase in grain size as a function of Cr content even if the sintering temperature was below the CrO eutectic melting temperature of 1950 K [26]. Furthermore, a maximum in grain size was observed at the Cr solubility limit [1], whereby further additions reduced the grain size. For sintering temperatures above the CrO liquid eutectic (1950 K [26]), Cr

additions well in excess of the solubility limit further increase the grain size, which is almost certainly due to liquid phase sintering. Nonetheless, a peak in grain size at the Cr solubility limit is present for all temperatures. Similar observations have been made for grain size as a function of dopant content in Ti-doped UO_2 [14]. Furthermore, Mg-doped UO_2 also exhibits enlarged grains [13] despite the lack of a eutectic and the MgO melting point (3125 K) being well in excess of sintering temperatures. As such, an open question exists regarding the mechanism responsible below the dopant solubility limit and/or below the eutectic temperature.

The defect concentrations in $UO_{2\pm x}$ and doped $UO_{2\pm x}$ are highly dependent on oxygen partial pressure and temperature. The relative ease with which U^{4+} may oxidize to U^{5+} results in a low energy charge compensation mechanism for the negatively charged hyper-stoichiometric defects v_U'''' and O_i''. Consequently, UO_2 can be easily oxidized to UO_{2+x} or U_4O_9, and even up to UO_3 through further oxidation to U^{6+}. However, it is not possible to reduce UO_2 to UO_{2-x} without heating the system to very high temperatures. Guéneau *et al.* [27] modelled the O/M ratio of $UO_{2\pm x}$ as a function of oxygen partial pressure and temperature by fitting to experimental data [28–42]. For a fixed oxygen partial pressure the O/M is found to reduce for increasing temperatures. A defect analysis [43] combining DFT defect energies with empirical potential vibrational entropy showed that uranium vacancies are suppressed at sintering temperatures due to reduction of UO_{2+x} to UO_2. Since grain growth kinetics are tied to vacancy-mediated uranium diffusivity, this can be prevented to some extent by using hyper-stoichiometric UO_{2+x} powder [44,45]. In this work mechanisms will be identified by which doping can also enhance uranium vacancy concentrations leading to high uranium diffusivity and faster grain growth kinetics via Equation (1).

The role of Cr in solution for grain growth has often been dismissed due to its assumed preference for the 3+ valance state and for accommodation at the U site, i.e. Cr_U' in Kröger-Vink notation [46] as used throughout this paper. This would result in negatively charged substitutional defects, which would suppress the concentration of the similarly charged U vacancies, v_U''''. The possibility of Cr accommodation as a positively charged interstitial defect has been proposed in the literature [47–49], however, it is not born out in atomistic simulations, which have in the past been used to predict the substitutional defect as more favourable [48]. Although uranium interstitials have been predicted to kick out Cr substitutional defects into an interstitial site [50], this is not representative of equilibrium conditions. These calculations used rigid Cr^{3+} models, which ignore the possibility that Cr can occupy multiple valence states given the d electrons in its outer shell. Cardinaels *et al.* [48] also concluded from comparison of XRD of Cr-doped UO_2 at room temperature with their atomistic calculations that Cr is in solution as a substitutional defect. However, vibrational entropy was not considered and may be important at the high sintering temperatures for UO_2 (1800–2200 K) and could lead to a change in the accommodation mechanism. Furthermore, the ability of dopants to access a wide range of valence states may allow for solution mechanisms that were precluded from previous simulations. In particular, valence states higher than 4+ would create positively charged substitutional defects at the uranium site. Otherwise, any valence states that allow cation dopants to occupy the interstitial site would be equally significant in the creation of positively charged defects and the resulting increase in uranium vacancy concentrations.

In this work, we have used a defect concentration analysis similar to that carried out on ThO_2 [51] and on $UO_{2\pm x}$ [43,52]. Similarly to Ref. [43], we have combined vibrational entropies from empirical calculations and defect energies from DFT+U. Defect concentrations have been analysed for UO_2 doped with Cr and Al. It will be shown that Cr exhibits lower valence states allowing it to access the interstitial site, whereas the high energy of Al reduction from 3+ to 2+ or 1+ prevents accommodation at the interstitial site. On this basis other dopants that can access lower valence states were also examined: the transition metals, Mn, Fe, Ti, and V, as well as the group 2 metal, Mg. The implications of increased uranium vacancy concentrations for enhanced grain growth and fission gas release are discussed.

2. Methodology

Defect calculations were carried out using the Vienna *ab initio* Simulation Package (VASP) [53–55]. The local density approximation (LDA) was applied to the exchange and correlation potential. The strongly correlated 5f electrons of uranium require the use of the LDA+U functional of Lichtenstein *et al.* [56]. The wave function was calculated using the projector augmented wave (PAW) method with core electrons accounted for within the frozen core approximation [57,58]. The values of $U = 4.5$ eV and $J = 0.51$ eV were taken from Dudarev *et al.* [59] in line with previous DFT studies on UO_2 [52,60–63]. Unfortunately, the introduction of the U parameter creates the additional challenge of metastable electronic states, which must be treated carefully, for example, through occupation matrix control [64] or U-ramping [65] to ensure the ground state configurations are achieved. As a number of the dopants studied are transition metals, U and J parameters have been applied to the highly correlated d electrons as follows: $U = 3.2$ eV and $J = 0.0$ eV for Cr [66], $U = 4.0$ eV and $J = 0.0$ eV for Mn [67,68], $U = 4.0$ eV and $J = 0.0$ eV for Fe [69], $U = 3.0$ eV and $J = 0.0$ eV for V [70], and $U = 5.0$ eV and $J = 1.0$ eV for Ti [71]. Spin-polarization was included with a 1-**k** antiferromagnetic ordering giving a good description of the lowest energy non-collinear 3-**k** ordering without including spin-orbit coupling, which due to computational cost prevents the use of sufficiently large supercells. This assumption is reasonable given that the Coulomb interaction was found to be 10–30 times higher than spin orbit coupling in 5f systems [72]. Furthermore, the 1-**k** antiferromagnetic ordering gives a good approximation of the high temperature paramagnetic ordering [73].

All DFT calculations were carried out using a 96 atom supercell consisting of a $2 \times 2 \times 2$ expansion of the UO_2 fluorite unit cell. Here we apply the U-ramping method to the U ions by carrying out 20 ionic steps at constant volume for each value of U from $U = J = 0.51$ eV to $U = 4.5$ eV at 0.5 eV increments. Subsequently, the ionic relaxation loop was converged to within 10^{-4} eV and the electronic relaxation loop to within 10^{-6} eV. Both ionic positions and cell parameters were relaxed during minimization. A plane-wave cut-off energy 500 eV was used. k-space integration was performed on a $2 \times 2 \times 2$ Monkhorst-Pack mesh [74] with Gaussian smearing of 0.05 eV. The interaction of charged defects with their periodic images has been corrected for through the Madelung energy [75,76]. The potential alignment correction was applied to the defective lattice energy using the approach of Taylor and Bruneval [77].

Host defects included in our analysis are v_U, v_O, and O_i. Uranium interstitials have been shown previously to have negligible concentrations [43,78] and have been omitted from this work. All charges ranging from neutral to formal have been included. Holes, $U_U^\bullet$, and electrons, U_U', have been treated in the same fashion as other charged defects by adding or removing electrons from the perfect supercell, allowing for structural relaxation associated with localised defects. DFT calculations for the host defects were carried out as part of previous work on undoped UO_2 [43], while DFT calculations for dopant defects have been conducted here for the first time using the same methodology. The following ranges of dopant defect charges have been considered: Cr_U'' to $^{\bullet\bullet}$, $Cr_i^\times$ to $^{\bullet\bullet\bullet\bullet\bullet\bullet}$,

Mn''_U to $^{\bullet\bullet}$, $Mn^\times_i$ to $^{\bullet\bullet\bullet\bullet\bullet}$, Fe''_U to $^{\bullet\bullet}$, $Fe^\times_i$ to $^{\bullet\bullet\bullet\bullet\bullet}$, V''_U to $^\bullet$, $V^\times_i$ to $^{\bullet\bullet\bullet\bullet}$, Ti''_U to $^\times$, $Ti^\times_i$ to $^{\bullet\bullet\bullet\bullet}$, Al''_U to $^\times$, $Al^\times_i$ to $^{\bullet\bullet\bullet}$, Mg''_U to $^\times$, and $Mg^\times_i$ to $^{\bullet\bullet}$. The DFT defect energies are summarised in Tables A1 and A2 in the Appendix.

The phonon vibrational modes of perfect and defective UO_2 have been calculated using the General Utility Lattice Program (GULP) [79] using the Busker potential [80]. A supercell consisting of a $4 \times 4 \times 4$ expansion of the fluorite unit cell was used for the calculation of phonon modes, ν_n, which were then used in the following summation to determine the vibrational entropy:

$$S_{vib} = k_B \sum_{n=1}^{3N-3} ln\left(\frac{h\nu_n}{k_B T}\right) + (3N - 3)k_B \tag{2}$$

where k_B is the Boltzmann constant, ν_n is the phonon frequency, T is the temperature, and h is Planck's constant. The derivative of equation (2) with respect to volume, $\frac{dS}{dV}$, has also been calculated for each defective and non-defective supercell and combined with the experimental thermal expansion of UO_2 [81] to determine the vibrational entropy.

Due to the lack of empirical parameters for different dopant charge states, we have initially used the $Cr^{3+} - O^{2-}$ parameters to calculate the entropy of $Cr_i^{\bullet\bullet\bullet}$ and Cr'_U with both cell volumes and atomic positions relaxed. However, the change in volume of the UO_2 lattice due to Cr defects varies significantly for different charge states and has an impact through the derivative of UO_2 vibration entropy as a function of volume, $\left(\frac{dS}{dV}\right)_{UO_2}$. This should not be confused with the correction for thermal expansion described above. In order to capture the effect of the change in defect volume associated with a Cr defect with valence, q, the following correction has been applied to the entropy of the Cr^{3+} defects:

$$S_{Cr^q} = S_{Cr^{3+}} + (V_{Cr^q} - V_{Cr^{3+}}) \cdot \left(\frac{dS}{dV}\right)_{UO_2} \tag{3}$$

where $V_{Cr^{3+}}$ is the defect volume of a Cr^{3+} defect (i.e. $Cr_i^{\bullet\bullet\bullet}$ and Cr'_U), and where $V_{Cr^{q+}}$ is the defect volume of a Cr^{q+} defect (e.g. if q = 2 then $Cr_i^{\bullet\bullet}$ and Cr''_U). Defect volumes have been determined from geometry relaxation in DFT. Tables A3 and A4 in the Appendix summarise the defect vibrational entropies and the vibrational entropy of the reference lattices. The DFT defect volumes used to adjust for non-formal dopant charges (see equation (3)) are shown in Table A5 in the Appendix.

It was found that the difference in vibrational entropy between Cr and Al for a given defect (substitutional or interstitial) was less than 0.1%. As such, for all dopants studied here (including Al for full consistency) we have used the interstitial and substitutional vibrational entropies and the defect volumes calculated for Cr (summarised in Table A4 and A5 in the Appendix). Similarly the vibrational entropies of all dopant reference oxides have been assumed to be the same as for Cr. To account for different numbers of O atoms per metal dopant atom in some reference oxides (e.g. VO_2), the vibrational entropies for CrO and Cr_2O_3 have been extrapolated as a function of O/M. This is a first order approximation that may slightly affect predictions of the most stable reference phases at low temperature. However, it will be shown in Section 3 that at the high temperatures relevant to sintering, MO and M_2O_3 reference oxides always dominate making this approximation suitable within the scope of this work, which focuses on grain growth at high temperatures.

The defect energy/entropy is the difference in energy/entropy between the defective and perfect supercells (see Tables A1-A4 in the Appendix). Using these the defect concentrations, c_i, are determined from an Arrhenius relationship:

$$c_i = m_i exp\left(\frac{-\Delta G_f^i}{k_B T}\right) \tag{4}$$

where m_i is the multiplicity, T is the temperature, and k_B is the Boltzmann constant. The free energy of defect formation is defined as:

$$\Delta G_f^i = \Delta E - T\Delta S_{vib} + \sum_\alpha n_\alpha \mu_\alpha + q_i \mu_e \tag{5}$$

where the defect energy, ΔE, is determined from DFT and the defect entropy, ΔS_{vib}, is determined from empirical potentials. n_α and μ_α are the number of species, α, and chemical potential of species, α, respectively that have been added to the system. q_i is the charge of the supercell containing the defect and μ_e is the electron potential.

The total Gibbs free energy of UO_2 can be defined in terms of the chemical potentials per formula unit of the constituent species:

$$\mu_{U(s)} + \mu_{O_2}(p_{O_2}, T) = \mu_{UO_{2(s)}} \tag{6}$$

where $\mu_{U(s)}$ and $\mu_{O_2}(p_{O_2}, T)$ are the chemical potentials of metal U and O_2 gas, respectively. In a similar manner to the defect energies (ΔE in equation (5)) the energies used to calculate the chemical potentials are taken from DFT, while vibrational entropy contributions are determined using the Busker potential. DFT is well known to provide a poor description of the O_2 dimer. Here the approach of Finnis et al. [84] is employed, whereby referencing the experimental formation energy of the oxide removes use of DFT to obtain the chemical potential of O via:

$$\Delta G_f^{UO_2}\left(p_{O_2}^\circ, T^\circ\right) = \mu_{UO_{2(s)}} - \mu_{U_{(s)}} - \mu_{O_{2(g)}}\left(p_{O_2}^\circ, T^\circ\right) \tag{7}$$

where $\Delta G_f^{UO_2}(p_{O_2}^\circ, T^\circ)$ is the experimental formation energy of UO_2 (−11.23 eV per UO_2 [85]). The temperature dependence of the O chemical potential is captured by using the ideal gas relations to extrapolate from $\mu_{O_{2(g)}}(p_{O_2}^\circ, T^\circ)$:

$$\mu_{O_{2(g)}}(p_{O_2}, T) = \mu_{O_{2(g)}}(p_{O_2}^\circ, T^\circ) + \Delta\mu(T) + \frac{1}{2}k_B T log\left(\frac{p_{O_2}}{p_{O_2}^\circ}\right) \tag{8}$$

and the rigid-dumbbell ideal gas for $\Delta\mu(T)$ is defined as:

$$\Delta\mu(T) = -\frac{1}{2}\left(S_{O_2}^\circ - C_P^\circ\right)(T - T^\circ) + C_P^\circ T log\left(\frac{T}{T^\circ}\right) \tag{9}$$

where $S_{O_2}^\circ = 0.0021$ eVK^{-1} is the molecular entropy at STP and $C_P^\circ = 7k_B = 0.000302$ eVK^{-1} is the constant pressure specific heat.

Using the framework discussed above the defect concentrations for a given set of conditions can be calculated by determining the electron potential, which is coupled to the charged defect formation energies, that ensures charge neutrality. The resultant defect concentrations can be expressed as a function of temperature or oxygen partial pressure and plotted to produce Brouwer diagrams. Generation of the Brouwer diagrams is done using the Defect Analysis Package [86]. For many of the dopants there are multiple reference oxides. The defect analysis was repeated using a different reference oxide each time for a given dopant, with the most stable reference state defined as that which has the lowest solubility in UO_2 for a given set of conditions. The following reference states have been considered: Cr_2O_3, Cr_3O_4, CrO, Mn_2O_3, Mn_3O_4, MnO, Fe_2O_3, Fe_3O_4, FeO, V_2O_5, VO_2, V_3O_5, V_2O_3, VO, TiO_2, Ti_2O_3, TiO, Al_2O_3, and MgO. While V_2O_3 [87], Ti_2O_3 [88], Cr_2O_3 [89] and Al_2O_3 [90] all

exhibit the corundum structure, Mn_2O_3 has the cubic bixbyite structure [91]. Fe_3O_4 has a cubic inverse spinel structure [92]. VO_2 [93] has distorted rutile-like monoclinic structure, V_3O_5 [94] exhibits the oxyvanite structure, and for V_2O_5 the structures listed in Ref. [95] were tested and the lowest energy used. TiO_2 exhibits the tetragonal rutile structure [96]. MgO, MnO, FeO, and VO all have the cubic rock salt structure [95,97,98]. However, for TiO the most stable structure is actually defective rock salt, $Ti_{1-x}O_{1-x}$. In this work the perfect rock salt energy of TiO is calculated and then adjusted using the energy of $Ti_{1-x}O_{1-x}$ relative to TiO from DFT calculations by Andersson *et al.* [99]. Although CrO only exists as a liquid, it has been treated as a rock salt solid here like the other oxides. It should be noted that above the eutectic temperature (1950 K) the free energy of the CrO liquid phase will be lower than for the theoretical rock salt. However, this is near the upper temperature limit of our calculations and the solubility of Cr is still expected to increase as a function of temperature.

3. Results and discussion

3.1. Cr and Al doping

Fig. 1a shows the defect concentrations for Cr-doped UO_2 from 500 K to 2000 K with an O partial pressure of 10^{-20} atm. The black line in Fig. 1a represents x in $UO_{2\pm x}$ and the dip that occurs at about 1700 K is due to the transition from low temperature UO_{2+x} to high temperature UO_{2-x}. The v_U'''' concentrations in the case of undoped UO_2 are also included using a dashed blue line. Given that our primary concern is the diffusivity of U due to its role in mass transport during grain growth and that U diffusion is vacancy assisted, the concentration of v_U'''' in the doped case compared to the undoped case is key. At low temperatures Cr is predicted to be accommodated at the uranium site in very small concentrations, indicating low solubility. The low concentrations result in no change in v_U'''' compared to the undoped case. Nonetheless, at low temperatures Cr^{3+} at the uranium site (Cr_U') is dominant relative to other valence states or Cr at other crystallographic sites. Although in the perfect fluorite lattice the uranium site is coordinated by 8 oxygen atoms, due to structural relaxation Cr exhibits 6-fold co-ordination when substituting the uranium ion (see Fig. 1a). This result is validated by x-ray absorption fine structure (EXAFS) spectroscopy experiments on Cr-doped UO_2 at room temperature,

which also shows Cr^{3+} with octahedral symmetry coordinated by 6 oxygen anions [6,7]. Furthermore, we predict Cr-O and U-O bond lengths of 2.13 Å and 2.38 Å, respectively, in reasonable agreement with experimental values of 2.02 Å and 2.36 Å, respectively [7].

For fixed oxygen partial pressure as the temperature increases the conditions become more reducing and the degree of excess oxygen decreases. Consequently, the concentrations of hyper-stoichiometric defects, O_i'' and v_U'''', decrease. Although the concentration of v_U'''' in undoped UO_2 decreases, increased sintering kinetics with temperature still occur due to faster hopping of the remaining v_U''''. However, in the case of Cr-doped UO_2, significant quantities of Cr are dissolved at the interstitial site at high temperatures. The Cr^{1+} ion is dominant at the interstitial site and the octahedron symmetry also seen for the substitutional site is maintained. Dopant accommodation at the interstitial site is a key result that, although hypothesised [47–49], has not been shown in previous work. Without accounting for the ability of the dopant to change valence state (e.g. from 3+ to 2+ to 1+) this mechanism would not have been identified. It is interesting that the charge effects of the interstitial defect seem to drive cations into a lower charge state, overcoming the size effects associated with the larger ionic radius of low valence ions. In this context it is worth noting the high stability of the O^{2-} interstitial in UO_2, which exhibits a greater ionic radius and lower valence than Cr^{1+}. Nonetheless, it is possible that for larger dopants or host systems with a smaller interstitial site the size effects might limit the transferability of this mechanism. As the $Cr_i^{\bullet}$ concentration exceeds that of $U_i^{\bullet}$ it becomes the dominant positively charged defect, which results in increased concentrations for all negatively charged defects in the system. Most importantly, the v_U'''' concentration for Cr-doped UO_2 exceeds that for undoped UO_2 for T > 1775 K and does so by over an order of magnitude at T = 2000 K, which would allow enhanced U mass transport and enlarged grains during sintering (see equation (1)). Note that upon cooling some Cr might be quenched in solution and is predicted to transition from the interstitial site to the U site and from Cr^{1+} to Cr^{3+}, which is consistent with experiments [6,7]. Alternatively, due to insolubility at low temperatures Cr_2O_3 precipitates might form, which has also been observed [1,8]. The ultimate balance between precipitation and quenching would depend on the cooling rate and Cr mobility.

Bourgeois *et al.* [1] showed that enhanced sintering can be achieve by Cr doping at 1800 K. The Cr interstitial mechanism proposed here can explain enhanced sintering at 1800 K (see
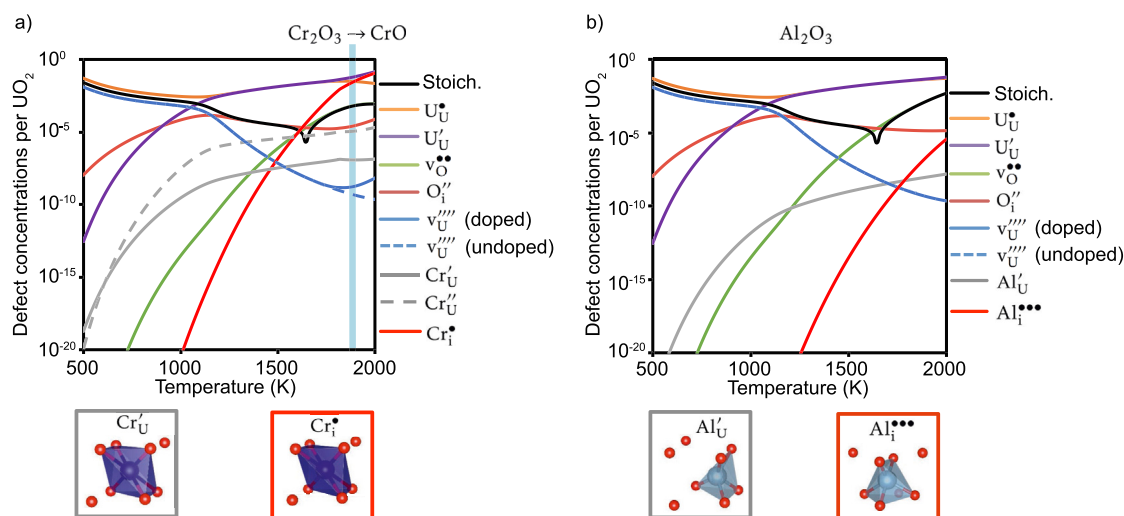

Fig. 1. Defect concentrations in a) Cr-doped and b) Al-doped $UO_{2\pm x}$ as a function of temperature (500–2000 K) for an O partial pressure of 10^{-20} atm. The most stable reference oxide for a given temperature is indicated above the figures. The crystallographic coordination of Cr and Al at the uranium and interstital sites is shown below the figures.

Fig. 1a), whereas the lowest possible temperature for the CrO liquid eutectic is 1950 K. Furthermore, by investigating grain size as a function of Cr content Bourgeois *et al.* found a peak at around the Cr solubility limit (700–1000 ppm) for all temperatures, and at temperatures above the eutectic they also found a secondary peak for Cr content well in excess of the solubility limit. We propose that formation of $Cr_i^\bullet$ and its effect on v_U'''' concentrations is responsible for the observed peak in grain size at the Cr solubility limit. For higher Cr content: i) if above the CrO eutectic temperature one would observe a secondary peak due to liquid phase sintering occurring in parallel to the interstitial mechanism or ii) if below the eutectic temperature solid secondary phases would pin grain boundaries and reduce grain size.

Starkly different behavior is predicted for Al-doped UO$_2$ (see Fig. 1b). Whereas Cr can transition to Cr^{1+} upon occupying the interstitial site at high temperature, Al does not. Al also prefers a 5-fold symmetry at both sites (see Fig. 1b). It appears that there is a preference of the interstitial site for a 1+ valence cation and the reluctance of Al to exhibit lower valance states seems to prohibit the formation of significant concentrations of Al interstitials. Consequently, $Al_i^{\bullet\bullet\bullet}$ never approaches similar concentrations to the dominant positively charged defect, $U_U^\bullet$, and no impact on v_U'''' concentrations is predicted for Al-doped UO$_2$ compared to undoped UO$_2$. This is in agreement with experiment where Al is shown not to enhance grain growth [15,49]. Rather, the formation of solid Al$_2$O$_3$ can inhibit grain growth by pinning [15]. There is evidence [5] that combinations of Al- and Cr-doping has an improved effect on grain size, however, this is beyond the scope of our point defect analysis.

The underlying difference between Al and Cr derives from their electronic structure. Cr is a transition metal, which means it can form stable ions with only a partially filled d shell. As a result the different valence states of Cr lie close in energy to each other, enabling it to transition to the lower charge states (i.e. 1+) favored by the interstitial site. On the other hand, Al has a 3s2 3p1 outer shell giving a strong preference to lose all 3 electrons in the outer shell and making the transition to charge states below 3+ unfavourable, which reduces the interstitial solubility at sintering temperatures. This opens the possibility that other transition (d electron) metals, which have chemistry that is not prohibitive of the lower charge states favored by the interstitial site, could enhance grain size through the same mechanism. It is important to select elements within this group that have small ionic radii so that the favourable charge effects of low valence interstitials is not overcome by size effects that would prefer the substitutional site.

3.2. Other transition metals: Ti, V, Mn, and Fe

The same defect analysis was carried out for some transition metals other than Cr. Fig. 2a shows that Mn behaves in a similar fashion to Cr, although there are now 3 important reference states (Mn$_2$O$_3$, Mn$_3$O$_4$, and MnO) compared to 2 for Cr (Cr$_2$O$_3$ and CrO). The transition from the substitutional defect to the interstitial defect occurs at 1400 K for Mn compared to 1500 K for Cr. The solubility of $Mn_i^\bullet$ is approximately 2 times that of $Cr_i^\bullet$ in the high temperature regime (>1800 K), resulting in 3.5–5 times greater v_U'''' concentrations. It is, therefore, anticipated that Mn-doped UO$_2$ will exhibit larger grains than Cr-doped UO$_2$ after sintering by utilising a higher Mn content in solution at interstitial sites [100]. Similarly to Cr, Mn is predicted to exhibit octahedral symmetry coordinated by 6 O at both the interstitial and substitutional sites (see Figs. 1a and 2a).

Fig. 2b shows that even though Fe_U'' transitions to $Fe_i^\bullet$ it is predicted to result in just a slight increase in the v_U'''' concentrations compared to undoped UO$_2$ up to 2000 K, which is due to the relative insolubility of Fe. Therefore, Fe is not expected to provide improved sintering with respect to Cr-doped UO$_2$, although grain size may be enhanced compared to undoped UO$_2$ for high sintering temperatures. We also note that Fe exhibits different coordination at both the uranium and interstitial sites compared to Mn and Cr. Fe_U'' has a 4-fold coordination asymmetric with respect to the perfect lattice uranium site. $Fe_i^\bullet$ exhibits 8-fold coordination at the interstitial site (see Fig. 2b). Despite the lower solubility the interstitial site still seems to enforce the 1+ charge state forming $Fe_i^\bullet$.

In agreement with experimental observations [11,14,15], Fig. 3 shows that enlarged grains can be expected in V- and Ti-doped UO$_2$ through the interstitial mechanism. V_U' and $V_i^\bullet$ have 5-fold coordination with significant deviation of V from the perfect lattice sites. Of all the dopants studied in this paper V exhibits the greatest increase in v_U'''' concentration. In fact the enhancement of negatively charged defects and suppression of positively charged defects is sufficient to reverse the transition from UO$_{2+x}$ to UO$_{2-x}$, such that a second dip at stoichiometry (black line) occurs. For Ti the dominant defects are Ti_U' and $Ti_i^{\bullet\bullet}$ both with 8-fold coordination

Fig. 2. Defect concentrations in a) Mn-doped UO$_2$ and b) Fe-doped UO$_2$ as function of temperature (500–2000 K) for an O partial pressure of 10^{-20} atm. The most stable reference oxide for a given temperature is indicated above the figures. The crystallographic coordination of Mn and Fe at the uranium and interstitial sites is shown below the figures.
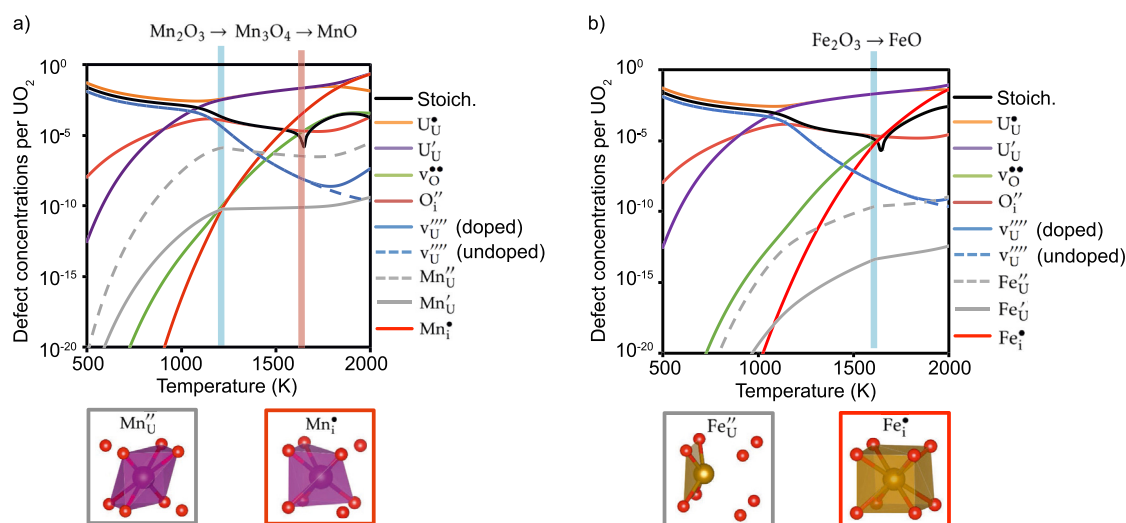
Fig. 3. Defect concentrations in a) Ti-doped UO₂ and b) V-doped UO₂) as function of temperature (500–2000 K) for an O partial pressure of 10^{-20} atm. The most stable reference oxide for a given temperature is indicated above the figures. The crystallographic coordination of Ti and V at the uranium and interstitial sites is shown below the figures.
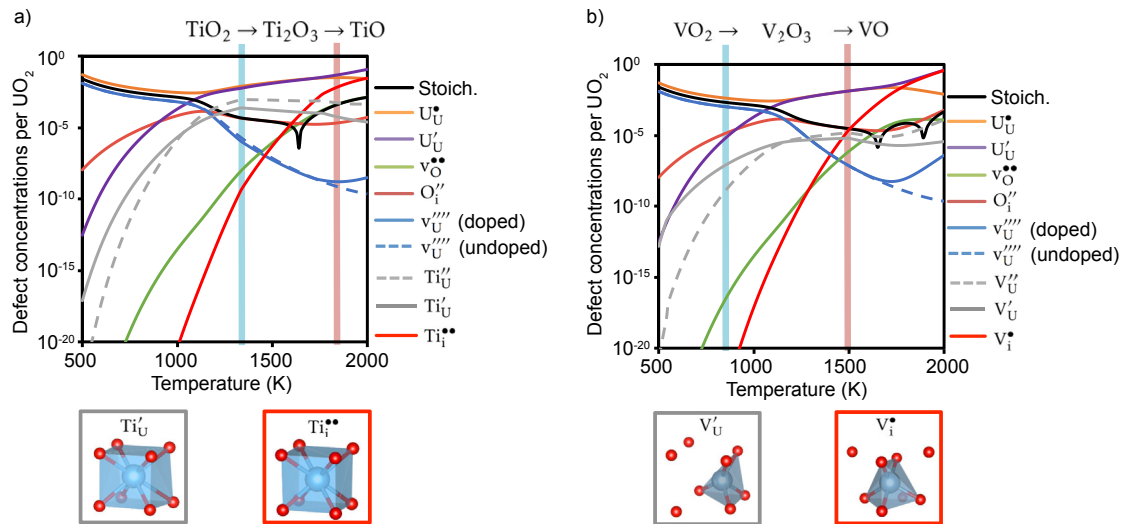
at the perfect lattice uranium and interstitial sites, respectively. It is interesting that for the Ti interstitial the 2+, rather than 1+, valence state is favourable. While this again highlights a preference for lower charge states at the interstitial site, it indicates that there is a difference in the electronic structure of Ti that tips the balance in favour of 2+. For all other transition metal dopants studied (Cr, Mn, and Fe) the transiton from 1+ to 2+ still leaves the d orbital partially filled (less favourable), whereas for Ti this transition leaves the d orbital empty (more favourable) with the outer shell consisting of just s electrons. Additionally, Ti being the larger of the transition metal dopants might be more favourable in a higher charge state that would reduce its volume and allow it to better fit the interstitial site. The results for the 2+ valence of the Ti interstitial demonstrates the ability of 2+ charged ions to occupy the interstitial site and motivates the investigation of group 2 metals (Section 3.3). Ainscough *et al.* [14] showed that below the titania-urania eutectic melting temperature (1875 K) grain growth peaks at the solubility limit, above which grain growth was inhibited by titania precipitates. Above the eutectic melting temperature further enhancement could be achieved above the solubility limit through liquid phase sintering. This supports our prediction that the interstitial dopant mechanism is important up to the solubility limit for Ti in UO₂ and/or below the eutectic melting temperature.

3.3. Group 2 metals: Mg

Given the importance of the lower valence states (e.g. 2+ for Ti) for accommodation at the interstitial site, group 2 elements are natural candidates for enhanced grain growth. Fig. 4 shows that Mg does indeed occupy the interstitial site in much higher concentrations than Al, although not to the same extent as Cr, Mn, Fe, Ti or V. For all dopants studied here (except Al) the monoxide is the most stable reference state at sintering temperatures. For Mg the high stability of MgO may contribute to limited solubility at high temperature, despite its natural affinity for the 2+ valence state associate with $Mg_i^{\bullet\bullet}$. Regardless, our results predict that Mg can be used to enhance grain size for high sintering temperatures, as has also been shown experimentally [11–13].

Similar to other dopants, at low temperatures Mg is predicted to occupy the U site. In contrast to the transition metals and Al, the solubility of Mg_U'' at low temperatures is relatively high. Consequently, when the concentration of the negatively charged Mg_U''
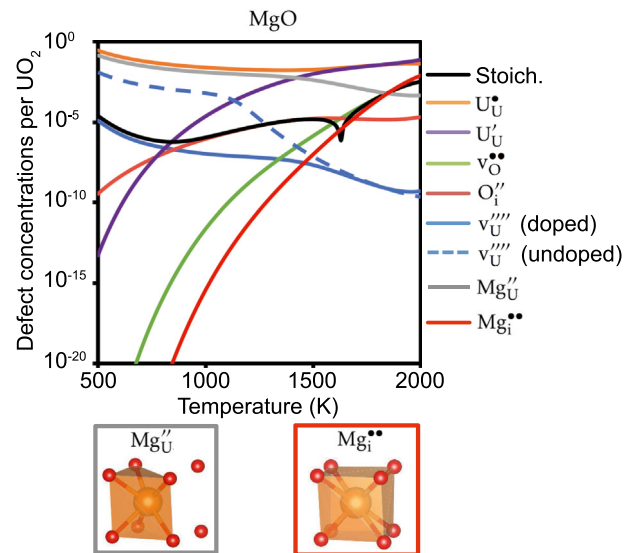

Fig. 4. Defect concentrations in Mg-doped $UO_{2\pm x}$ as function of temperature (500–2000 K) for an O partial pressure of 10^{-20} atm. The most stable reference oxide for a given temperature is indicated above the figures. The crystallographic coordination of Mg at the uranium and interstital sites is shown on the right hand side.

approaches that of other negatively charged defects (v_U''' and O_i'') it begins to suppress the v_U''' concentration. Unlike the other dopants studied, which dissolve directly onto the interstitial site, Mg transitions from the substitutional to the interstitial site. Experimental work by Fujino *et al.* [13] showed that Mg can be accommodated at both the uranium and interstitial sites with a bias towards the interstitial at high temperatures, in line with our calculations.

3.4. Discussion

Throughout the results section it has become apparent that the ability of a dopant to occupy lower valence states (1+ or 2+) underpins the formation of positively charged interstitial defects. The relative stability of the interstitial and the substitutional dopants is key for the ability of dopants to introduce positive charge to system.

This is examined by fitting Arrhenius functions to the ratio of interstitials to substitutional defects, $\frac{[X_i]}{[X_U]}$, taken from the defect concentrations (summed over all charge states) shown in Figs. 1–4. There are three distinct temperature regimes for $\frac{[Cr_i]}{[Cr_U]}$ to which we have fitted three Arrhenius functions, in Fig. 5. The transition between two regimes is governed by a change in the dominant charge compensating mechanism. In the case of Cr for low temperatures v_U'''' and $U_U^\bullet$ dominate, for intermediate temperatures U_U' and $U_U^\bullet$ dominate, and for high temperatures $Cr_i^\bullet$ and U_U' dominate. The same analysis has been carried out for all the dopants and the coefficients for each regime are summarised in Table 1. The three regimes for Cr can be generalised to Mn, Ti, V, and Fe, such that the transition between the low and intermediate regimes is independent of the dopant and occurs at the same temperature (1080 K) but the transition from the intermediate to the high regime is commensurate with the temperature at which enhancement of v_U'''' concentrations occurs for a given dopant. For Al the high
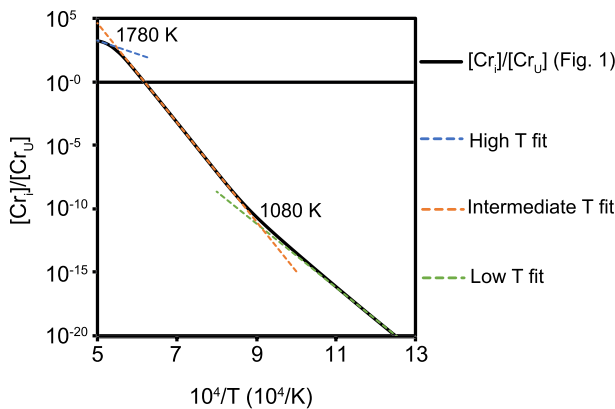

Fig. 5. The fraction of Cr interstitial defect concentrations to substitutional defect concentrations (summed over all charge states), $\frac{[Cr_i]}{[Cr_U]}$, calculated from Fig. 1a) is shown by the solid black line. The dashed lines indicate Arrhenius fits to $\frac{[Cr_i]}{[Cr_U]}$ in three different regimes. The parameters for the Arrhenius fits are shown in Table 1.

Table 1
The relative stability of interstitial vs substitutional dopants is summarised by fitting an Arrhenius function $\left(A\exp\frac{-B}{k_bT}\right)$ to the data for $\frac{[X_i]}{[X_U]}$ (summed over all charges) from Figs. 1–4 $X =$ Cr, Al, Mn, Fe, Ti, V, Mg.

Dopant, X (Temperature range)	A (no units)	B (eV)
Cr (600–1080 K)	3.049×10^{11}	4.993
Cr (1080–1780 K)	1.425×10^{24}	7.754
Cr (1780–2000 K)	3.362×10^{8}	2.094
Al (600–1080 K)	1.305×10^{9}	5.188
Al (1080–2000 K)	9.000×10^{22}	8.255
Mn (600–1080 K)	1.144×10^{13}	4.993
Mn (1080–1700 K)	1.477×10^{24}	6.866
Mn (1700–2000 K)	1.943×10^{8}	1.268
Fe (600–1080 K)	1.149×10^{13}	3.817
Fe (1080–1880 K)	1.432×10^{24}	6.298
Fe (1880–2000 K)	4.627×10^{13}	2.396
Ti (600–1080 K)	1.909×10^{13}	5.582
Ti (1080–1760 K)	2.787×10^{23}	7.923
Ti (1760–2000 K)	9.459×10^{10}	3.503
V (600–1080 K)	1.403×10^{14}	5.011
V (1080–1730 K)	3.215×10^{24}	7.250
V (1730–2000 K)	6.001×10^{6}	1.155
Mg (600–1430 K)	1.763×10^{12}	5.115
Mg (1430–1980 K)	3.279×10^{20}	7.457
Mg (1980–2000 K)	1.786×10^{15}	5.382

temperature regime does not exist because $Al_i^{\bullet\bullet\bullet}$ is never a dominant defect. On the other hand, Mg replaces v_U'''' as the dominant negatively charged defect in the low temperature regime. The resulting transition to the intermediate (U_U' and $U_U^\bullet$ dominated) regime now occurs at 1430 K.

It is this extrinsic positive charge created by interstitial formation that increases the concentrations of all negatively charged host defects including the v_U'''' concentration, which increases the U diffusivity. Fig. 6a shows the v_U'''' concentrations as a function of temperature in undoped and (Mg/Al/Ti/V/Cr/Mn/Fe)-doped UO_2 from Figs. 1–4 but zoomed in at temperatures relevant to sintering and the centerline fuel pellet temperature. It is more clearly seen in Fig. 6a that Fe and Mg only slightly enhance the v_U'''' concentrations, i.e. with respect to undoped UO_2 at 2000 K Fe and Mg enhance v_U'''' by a factor of 3 and 2, respectively. This is relatively limited when compared to Mn and Cr, which enhance v_U'''' concentrations by $1-2$ orders of magnitude.

Enlarged grains are considered to increase plasticity (through the Hall-Petch effect [101,102]) and reduce fission gas release (by increasing the distance of the rate limiting intragranular diffusion step). Assuming that initial grain size is much smaller than the final grain size ($\overline{G} \gg \overline{G}_0$) and ideal (i.e. bulk diffusion dominated) grain growth, Equation (1) can be expressed as:

$$\overline{G}^2 = t \cdot k_0 \exp\left(\frac{-Q}{k_BT}\right) \tag{10}$$

For diffusion dominated grain growth, uranium diffusion is the rate limiting step, whereby $k_0\exp\left(\frac{-Q}{k_BT}\right)$ is proportional to the uranium diffusivity, which is in turn proportional to the concentration of v_U'''' assuming the mobility of an individual vacancy is unchanged. It is possible, therefore, to express the average grain size of doped UO_2, $\overline{G}_{doped}$, relative to that of undoped UO_2, $\overline{G}_{undoped}$, as:

$$\frac{\overline{G}_{doped}}{\overline{G}_{undoped}} = \sqrt{\frac{[v_U'''']_{doped}}{[v_U'''']_{undoped}}} \tag{11}$$

where $[v_U'''']_{doped}$ and $[v_U'''']_{undoped}$ are the uranium vacancy concentrations for doped and undoped UO_2 shown in Fig. 6a. $\frac{\overline{G}_{doped}}{\overline{G}_{undoped}}$ is shown in Fig. 6b. Note that for non-ideal grain growth mechanisms $n > 2$ and the extent of grain enhancement in real life might be not as great as shown in Fig. 6b. The predictions made here for uranium vacancy concentrations can be fed into sintering simulations for more complete predictions of grain growth.

An implication of V, Ti, Cr and Mn dopants is that they might result in increased v_U'''' concentrations at reactor operating temperatures, which is an important parameter for the diffusivity of fission gas [103–105]. Hence, it is expected that the bulk fission gas diffusivity would be increased (especially in the central region of the fuel) effectively competing with larger grain size for the amount of fission gas ultimately released from grain boundaries. This hypothesis is supported by the observation of Killeen et al. [4] that Cr-doped UO_2 has higher Kr diffusivity than undoped UO_2 at 1775 K. Furthermore, from fission gas release measurements Kashibe and Une [47] report that above 1500 K Cr-doped UO_2 has higher Xe diffusivity than undoped UO_2 (the converse is true below 1500 K). To explain this behavior they hypothesised that indeed a Cr interstitial defect was responsible and, furthermore, 1500 K is commensurate with our prediction of the transition between Cr substitutional and interstitial defects, even if we do not predict enhanced v_U'''' concentrations at 1500 K.. Kashibe and Une [47] also
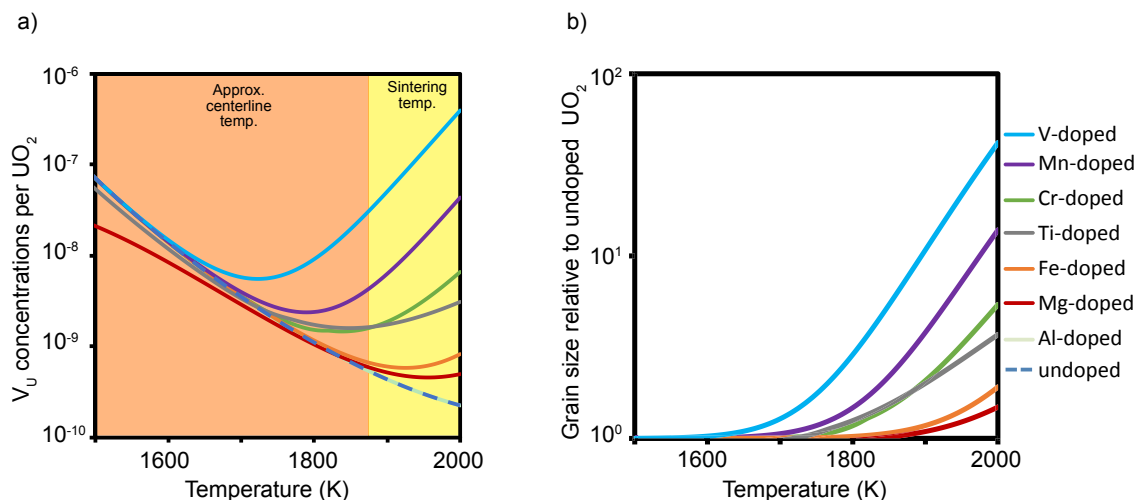
Fig. 6. a) Comparison of the v_U'''' concentrations in undoped and (Mg/Al/Ti/V/Cr/Mn/Fe)-doped UO_2 at temperatures relevant to the fuel centreline and for sintering with an O partial pressure of 10^{-20} (atm). b) The grain size enhancement with respect to undoped UO_2 assuming diffusion dominated grain growth.

report that Al- and Mg-doping have no effect on Xe diffusivity. Une *et al.* [45] report that additions of 0.5 wt% Nb and 0.2 wt% Ti result in Xe diffusivity enhancement of factors of 50 and 7, respectively, supporting our prediction of a common interstitial-based v_U'''' enhancement mechanism for a wide range of dopants. The relationship between enhanced fission gas diffusivity and enlarged grains, and the integrated role on fission gas release, is a complicated issue that must be addressed by longer length and time scale simulations, not to mention additional experiments. Nonetheless, as a consequence of enhanced fission gas diffusivity we do not expect the full benefit of enlarged grains to be attained. Similarly, for V−doped UO_2 even greater grain enlargement is expected compared to Ti-, Cr- and Mn-doped UO_2, however we predict that fission gas diffusivity will also be greater if sufficiently high temperatures occur in the pellet during reactor operation. Regardless, large grain size in doped UO_2 would still provide enhanced plasticity with benefits to the mechanical interactions between the pellet and the cladding.

The transferability of this interstitial mechanism across a wide range of transition and group 2 metal dopants opens the possibility that it could also be transferable across a range of host systems, similar to UO_2. The transferability of this mechanism depends on the favourable low charge state effect overcoming the size effect limitations (associated with the interstitial site given the larger radii of low valence ions). We anticipate this work will form the basis for future studies on a wider body of materials. For example, the role of dopants in grain growth of doped CeO_2 is unclear [106–108].

4. Conclusions

Enlarged UO_2 grain size is thought to provide better nuclear fuel performance through increased plasticity and improved fission gas retention. Dopants have been widely used to provide enhanced grain growth during sintering. While liquid phase sintering has been often touted in the literature, there are experimental observations that lend themselves to the idea that there may be an additional grain growth mechanism during sintering. By reexamining the role of dopants in solution in UO_2 with relaxed assumptions of dopant valence state, we predict that an interstitial solution mechanism contributes to enhanced grain size in a number of doped systems. In particular, this mechanism increases v_U'''' concentrations, thus, resulting in higher U diffusivity during sintering (i.e. faster grain growth).

The defect analysis was carried out using DFT defect energies and empirical potential vibrational entropies on the solution of Cr, Al, Mn, Fe, Ti, V, and Mg into UO_2 as a function of temperature. Negatively charged substitutional defects were predicted to dominate for all dopants over a large temperature range. The concentrations of these defects are sufficiently low for Cr, Al, Mn, Fe, Ti, and V as to not affect the v_U'''' concentrations compared to undoped UO_2. Mg on the other hand forms Mg_U'' at significant enough concentrations to suppress v_U'''' concentrations at low temperatures.

At temperatures relevant to sintering, all dopants studied (except Al) were predicted to form 1+ or 2+ charged interstitial defects at different concentrations depending on the dopant. V-doped UO_2 was predicted to have the highest solubility at the interstitial site followed by Mn, Ti and Cr. Consequently, Ti, V, Cr, and Mn greatly enhance the v_U'''' concentrations compared to undoped UO_2. Fe and Mg also enhance the v_U'''' concentration but to a lesser extent, while Al has no effect.

Enhanced v_U'''' concentrations in doped fuel will also increase fission gas diffusivity at operating temperatures (especially near the centerline). The extent to which enhanced diffusivity competes with larger grains for fission gas retention is unclear and requires further consideration. However, we have shown an important aspect of the problem, which is that the same mechanism governs both grain growth kinetics and fission gas diffusivity.

Appendix

Here we provide the defect data from DFT and empirical potential calculations that were used in the defect analysis carried out in the main body of the paper. The DFT lattice energies have been corrected for the interactions between the charged defect with its

periodic images through the Madelung energy such that [75,76]:

$$E_\infty = E_L + \frac{q^2\alpha}{2\varepsilon L} \tag{12}$$

where E_∞ is the lattice energy in the dilute limit, E_L is the lattice energy in a supercell of length L, and q is the supercell charge. $\alpha = 2.837$ is the Madelung constant of a point charge q placed in a homogeneous background charge $-q$ and $\varepsilon = 22$ is the dielectric constant taken from experiment [109]. A potential alignment correction to the defect lattice energies, $\Delta\Phi$, due to the shift in band structure of the defective supercell with respect to the perfect supercell was calculated as [77]:

$$\Delta\Phi = \left\langle \phi_{KS}^{bulk} \right\rangle - \left\langle \phi_{KS}^{defect} \right\rangle \tag{13}$$

where $\left\langle \phi_{KS}^{bulk} \right\rangle$ and $\left\langle \phi_{KS}^{defect} \right\rangle$ are the average Kohn-Sham potentials in the perfect and defective supercells, respectively. The charge and potential alignment corrected defect energies are summarised in Table A1 for host defects and in Table A2 for dopant defects.

The values of S_{vib} for various defects have been calculated from equation (2) with the phonon modes predicted by the Busker potential. The derivative of equation (2) with respect to volume, $\frac{dS}{dV}$, for the defective and perfect supercells has been used to adjust for the experimental thermal expansion [81]. The difference between the perfect and defective supercells, ΔS_{vib}, is summarised in Tables A3 and A4 alongside the vibrational entropy of the reference oxides. Table A5 shows the defect volumes for interstitial and substitutional Cr defects with various charge states. The difference in volume relative to the Cr^{3+} defects has been used with $\left(\frac{dS}{dV}\right)_{UO_2} = 0.341\ k_B/\text{Å}^3$ to modify the defect entropies in Table A4 to determine the entropy for non-formally charged defects (equation (3)).

Table A1
DFT defect energies for host (U and O) defects with various charges [43]. The energies have been corrected for the interaction of the charged defect with its periodic images using Equation (12) and corrected for potential alignment using Equation (13). The DFT energy of perfect UO_2 per formula unit is -31.915 eV.

Effective charge	Defect energy (eV)						
	−4	−3	−2	−1	0	+1	+2
Non-defective (eV)	−	−	−	10.026	0.000	−8.527	−
V_O (eV)	−	−	−	−	12.024	2.243	−7.321
O_i (eV)	−	−	11.546	2.703	−5.945	−	−
V_U (eV)	53.336	44.774	36.294	27.798	19.467	−	−

Table A2
DFT defect energies for dopant defects with various charges. The energies have been corrected for the interaction of the charged defect with its periodic images using Equation (12) and corrected for potential alignment using Equation (13).

Effective charge	Defect energy (eV)								
	−2	−1	0	+1	+2	+3	+4	+5	+6
Cr_i	−	−	−3.691	−13.778	−22.885	−31.354	−39.775	−48.384	−56.460
Cr_U	26.232	17.287	8.894	0.498	−8.021	−	−	−	−
Al_i	−	−	0.122	−10.001	−19.781	−29.563	−	−	−
Al_U	28.607	18.861	10.526	−	−	−	−	−	−
Mn_i	−	−	−2.724	−12.797	−21.494	−29.953	−38.293	−46.655	−55.106
Mn_U	28.106	19.539	8.981	3.721	−2.706	−	−	−	−
Fe_i	−	−	−2.925	−13.068	−21.693	−30.093	−38.735	−47.106	−55.608
Fe_U	28.400	19.856	11.338	2.817	−5.499	−	−	−	−
Ti_i	−	−	−3.615	−13.751	−23.533	−32.080	−40.629	−	−
Ti_U	25.619	16.135	7.548	−	−	−	−	−	−
V_i	−	−	−4.559	−14.521	−23.830	−32.469	−41.012	−49.240	−
V_U	26.123	16.533	8.022	−0.370	−	−	−	−	−
Mg_i	−	−	1.046	−8.891	−18.559	−	−	−	−
Mg_U	29.652	21.158	12.620	−	−	−	−	−	−

Table A3
Using the Busker potential [80], the change in lattice entropy of UO_2 due to a host defect (ΔS_{vib}) and the vibrational entropy of the UO_2 lattice per formula unit, which is used to calculate the chemical potential of the U atoms.

T (K)	Lattice entropy	Defect entropy for host defects (ΔS_{vib})					Reaction entropy	
	UO_2 (k_B) [43]	v_O (k_B) [43]	O_i (k_B) [43]	v_U (k_B) [43]	$U_U^\bullet$ (k_B) [43]	U_U' (k_B) [43]	SD (k_B)	OFP (k_B)
400	7.785	−0.245	8.305	2.410	−1.195	4.309	9.714	7.959
600	11.531	−1.544	9.705	1.085	−1.149	4.243	9.528	8.060
800	14.219	−2.109	10.752	0.103	−1.103	4.177	9.343	8.160
1000	16.328	−3.242	11.606	−0.686	−1.057	4.110	9.157	8.262
1200	18.069	−3.872	12.339	−1.353	−1.010	4.043	8.972	8.364
1400	19.559	−4.419	12.989	−1.936	−0.964	3.976	8.785	8.467
1600	20.863	−4.903	13.577	−2.458	−0.917	3.908	8.590	8.570
1800	22.026	−5.341	14.119	−2.933	−0.870	3.840	8.410	8.673
2000	23.078	−5.742	14.624	−3.371	−0.822	3.771	8.222	8.882

Table A4

Using the Busker potential [80], the change in lattice entropy of UO_2 due to a Cr defect (ΔS_{vib}) and the vibrational entropy of the reference lattices (per Cr atom) used in the calculation of the chemical potential of the dopant atoms is shown per formula unit.

T (K)	Reference oxide entropy per Cr		Defect entropy for Cr defects (ΔS_{vib})	
	Cr_2O_3 (k_B)	CrO (k_B)	Cr'_U (k_B)	$Cr_i^{\bullet\bullet\bullet}$ (k_B)
400	4.059	5.221	1.360	8.767
600	7.126	7.672	1.132	10.114
800	9.309	9.418	0.903	11.108
1000	11.001	10.778	0.673	11.909
1200	12.405	11.892	0.442	12.588
1400	13.588	12.839	0.209	13.184
1600	14.618	13.662	−0.024	13.718
1800	15.529	14.391	−0.259	14.205
2000	16.347	15.046	−0.495	14.656

Table A5

The change in lattice volume due to geometry optimization of Cr defects with different charge states, q. The difference in volume with respect to the formally charged defects (shown in parentheses) is used in conjunction with $\left(\frac{dS}{dV}\right)_{UO_2} = 0.341\ k_B/\text{Å}^3$ to adjust the entropy for Cr defects with non-formal charges (Equation (3)).

Cr valence (q)	Defect	Defect volume (Å^3)	Defect	Defect volume (Å^3)
0	–	–	$Cr_i^{\times}$	9.76 (32.88)
I	–	–	$Cr_i^{\bullet}$	−3.02 (20.10)
II	Cr''_U	13.66 (15.90)	$Cr_i^{\bullet\bullet}$	−15.80 (7.32)
III	Cr'_U	−2.24 (0.00)	$Cr_i^{\bullet\bullet\bullet}$	−23.12 (0.00)
IV	$Cr_U^{\times}$	−12.94 (−10.70)	$Cr_i^{\bullet\bullet\bullet\bullet}$	−36.27 (−13.15)
V	$Cr_U^{\bullet}$	−26.48 (−24.24)	$Cr_i^{\bullet\bullet\bullet\bullet\bullet}$	−48.22 (−25.10)
VI	$Cr_U^{\bullet\bullet}$	−37.13 (−34.89)	$Cr_i^{\bullet\bullet\bullet\bullet\bullet\bullet}$	−59.71 (−36.59)

References

[1] L. Bourgeois, P. Dehaudt, C. Lemaignan, A. Hammou, Factors governing microstructure development of Cr_2O_3-Doped UO_2 during sintering, J. Nucl. Mater. 297 (2001) 313—326.

[2] V. Peres, L. Favergeon, M. Andrieu, J.C. Palussière, J. Balland, C. Delafoy, M. Pijolat, High temperature chromium volatilization from Cr_2O_3 powder and Cr_2O_3-Doped UO_2 pellets in reducing atmospheres, J. Nucl. Mater. 423 (2012) 93—101.

[3] A.R. Massih, Effects of Additives on Uranium Dioxide Fuel Behavior, Strålsäkerhets Myndigheten, 2014, 21ISSN:2000-0456.

[4] J.C. Killeen, Fission gas release and swelling in UO_2 doped with Cr_2O_3, J. Nucl. Mater. 88 (1980) 177—184.

[5] J. Arborelius, K. Backman, L. Hallstadius, M. Limbäck, J. Nilsson, B. Rebemsdorff, G. Zhou, K. Kitano, R. Löfström, G. Rönnberg, Advanced doped UO_2 pellets in LWR applications, J. Nucl. Sci. Technol. 43 (2006) 967—976.

[6] C. Riglet-Martial, P. Martin, D. Testemale, C. Sabathier-Devals, G. Carlot, P. Matheron, X. Iltis, U. Pasquet, C. Valot, C. Delafoy, R. Largenton, Thermodynamics of chromium in UO_2 fuel: a solubility model, J. Nucl. Mater. 447 (2014) 63—72.

[7] C. Mieszczynski, G. Kuri, J. Bertsch, M. Martin, C.N. Borca, C. Delafoy, E. Simoni, Microbeam X-ray absorption spectroscopy study of chromium in large-grain uranium dioxide fuel, J. Phys. Condens. Matter 26 (2014) 355009.

[8] Z. Kuri, C. Mieszczynski, M. Martin, J. Bertsch, C.N. Borca, C. Delafoy, Local atomic structure of chromium bearing precipitates in chromia doped uranium dioxide investigated by combined micro-beam X-ray diffraction and absorption spectroscopy, J. Nucl. Mater. 449 (2014) 158—167.

[9] H. Assmann, W. Dörr, G. Gradel, G. Maier, M. Peehs, Doping UO_2 with niobia - beneficial or not? J. Nucl. Mater. 98 (1981) 216—220.

[10] J.C. Killeen, The effect of additives on the irradiation behaviour of UO_2, J. Nucl. Mater. 58 (1975) 39—46.

[11] T. Fujino, T. Shiratori, N. Sato, K. Fukuda, K. Yamada, H. Serizawa, Solubility of magnesium in uranium dioxide, J. Nucl. Mater. 297 (2001) 176—205.

[12] P.T. Sawbridge, C. Baker, R.M. Cornell, K.W. Jones, D. Reed, J.B. Ainscough, The

irradiation performance of magnesia-doped UO_2 fuel, J. Nucl. Mater. 95 (1980) 119—128.

[13] T. Fujino, S. Nakama, N. Sato, K. Yamada, K. Fukuda, H. Serizawa, T. Shiratori, Solubility of magnesium in uranium dioxide, J. Nucl. Mater. 246 (1997) 150—157.

[14] J.B. Ainscough, F. Rigby, S.C. Osborn, The effect of titania on grain growth and densification of sintered UO_2, J. Nucl. Mater. 52 (1974) 191—203.

[15] R.M. Leckie, E.P. Luther, A.T. Nelson, Report on Evolutionary Enhancements to UO_2 Pellets, LANL Milestone Report, 2013. M3FT-13LA020206.

[16] R.F. Canon, J.T.A. Roberts, R.J. Beals, Deformation of UO_2 at high temperatures, Am. Ceram. Soc. 54 (1971) 105—112.

[17] T. Tachibana, H. Furuya, M. Koizumi, Dependence on strain rate and temperature shown by yield stress of uranium dioxide, J. Nucl. Sci. Technol. 13 (1976) 497—502.

[18] R.W. Rice, Effects of environment and temperature on ceramic tensile strength-grain size relations, J. Mater. Sci. 32 (1997) 3071—3087.

[19] L. Bourgeois, P. Dehaudt, C. Lemaignan, J.P. Fredric, Pore migration in UO_2 and grain growth kinetics, J. Nucl. Mater. 295 (2001) 73—82.

[20] J.E. Burke, D. Turnbull, Recrystallization and grain growth, Prog. Met. Phys. 3 (1952) 220.

[21] M.P. Anderson, D.J. Srolovitz, G.S. Grest, P.S. Sahni, Computer simulation of grain Growth-I. Kinetics, Acta Metall. 32 (1984) 783—791.

[22] W.D. Kingery, B. Francois, Grain growth in porous compacts, J. Am. Ceram. 48 (1965) 546.

[23] F.A. Nichols, Theory of grain growth in porous compacts, J. Appl. Phys. 37 (1966) 4599.

[24] R.J. Brook, Treatise Materials Science Technology, Ceramics, vol. 9, Academic Press, New York, 1979.

[25] J.R. MacEwan, J. Hayashi, Grain growth in UO_2, III. Some factors influencing equiaxed grain growth, Proc. Br. Ceram. Soc. 7 (1965) 245.

[26] C. Riglet-Martial, P. Martin, D. Testemale, C. Sabathier-Devals, G. Carlot, P. Matheron, X. Lltis, U. Pasquet, C. Valot, C. Delafoy, R. Largenton, Thermodynamics of chromium in UO_2 fuel: a solubility model, J. Nucl. Mater. 447 (2014) 63—72.

[27] C. Guéneau, M. Baichi, D. Labroche, C. Chatillon, B. Sundman, Thermodynamic assessment of the uranium-oxygen system, J. Nucl. Mater. 304 (2002) 161—175.

[28] M. Tetenbaum, P.D. Hunt, High-temperature thermodynamic properties of oxygen-deficient urania, J. Chem. Phys. 49 (1968) 4739.

[29] A. Pattoret, PhD Thesis, University Libre De Bruxelles 1969.

[30] N.A. Javed, Thermodynamic study of hypostoichiometric urania, J. Nucl. Mater. 43 (1972) 219.

[31] P. Gerdanian, M. Dodé, J. Extrait, Étude Thermodynamique des Oxydes UO_{2+x}, J. Chim. Phys. 62 (1965) 171—184.

[32] A. Kotlar, P. Gerdanian, M. Dodé, Détermination des Pressions Partielles d'Oxygène en Équilibre avec les Oxydes Non-Stoechiométriques du Système U-O pour 1080 °C < Θ < 1150 °C et 2,19 < O/U < 2,63, J. Chim. Phys. 64 (1967) 862—868.

[33] A. Kotlar, P. Gerdanian, M. Dodé, Détermination des Pressions Partielles d'Oxygène en Équilibre avec les Oxydes Non-Stoechiométriques du Système U-O pour 1050 °C < Θ < 1150 °C et 2,19 < O/U < 2,63, J. Chim. Phys. 64 (1967) 1135—1144.

[34] A. Kotlar, P. Gerdanian, M. Dodé, Détermination des Limites de Phases du Système U-O par Transfert d'Oxygène. - diagramme de Phase pour la Région 2,19 < O/U < 2,63 et 1080 < Θ°C < 1200, J. Chim. Phys. 65 (1968) 687—691.

[35] K. Hagemark, M. Broli, Equilibrium oxygen pressures over the non-stoicheiometric uranium oxides UO_{2+x} and U3O8-z at higher temperatures, J. Inorg. Nucl. Chem. 28 (1966) 2837—2850.

[36] P.E. Blackburn, Oxygen dissociation pressures over uranium oxides, J. Phys. Chem. 62 (1958) 897.

[37] L.E.J. Roberts, A.J. Walter, Equilibrium pressures and phase relations in the uranium oxide system, J. Inorg. Nucl. Chem. 22 (1961) 213.

[38] S. Aronson, J. Belle, Oxidation and corrosion of uranium dioxide, J. Phys. Chem. 35 (1961) 1382.

[39] D.L. Marchidan, S. Matei, Rev. Roum. Chem. 20 (1975) 1365.

[40] Y. Saito, Nonstoichiometry in uranium dioxide, J. Nucl. Mater. 51 (1974) 112—125.

[41] K. Kuikkola, High-temperature electrochemical study of uranium oxides in the UO_2-U3O8 region, Acta Chem. Scand. 16 (1962) 327—345.

[42] T. Nakamura, T. Fujino, Thermodynamic study of UO_{2+x} by solid state emf technique, J. Nucl. Mater. 149 (1987) 80—100.

[43] M.W.D. Cooper, S.T. Murphy, D.A. Andersson, The defect chemistry of $UO_{2\pm x}$ from atomistic simulations, J. Nucl. Mater. (2018), https://doi.org/10.1016/j.jnucmat.2018.02.034. In Press.

[44] P. Dehaudt, L. Bourgeois, H. Chevral, Activation energy of UO_2 and UO_{2+x} sintering, J. Nucl. Mater. 299 (2001) 250—257.

[45] K. Une, I. Tanabe, M. Oguma, Effects of additives and the oxygen potential on the fission gas diffusion in UO_2 fuel, J. Nucl. Mater. 150 (1987) 93—99.

[46] F.A. Kröger, H.J. Vink, Relations between the concentrations of imperfections in crystalline solids, Solid State Phys. 3 (1956) 307—435.

[47] S. Kashibe, K. Une, Effect of additives (Cr_2O_3, Al_2O_3, SiO_2, MgO) on diffusional release of 133Xe from UO_2 fuels, J. Nucl. Mater. 254 (1998) 234—242.

[48] T. Cardinaels, K. Govers, B. Vos, S. Van den Berghe, M. Verwerft, L. de Tollenaere, G. Maier, C. Delafoy, Chromia doped UO_2 fuel: investigation of the lattice parameter, J. Nucl. Mater. 424 (2012) 252—260.

[49] D.R. Costa, F.J. Ezequiel, R. Gonzaga, S.H. Bernardelli, Individual Influence of Al_2O_3 and Nb_2O_5 on Grain Growth of UO_2 Sintered Pellets Manufactured at INB, International Atlantic Conference (INAC 2013), 2013, ISBN 978-85-99141-05-2, http://www.iaea.org/inis/collection/NCLCollectionStore/_Public/45/087/45087491.pdf.

[50] Z. Guo, R. Ngayam-Happy, M. Krack, A. Pautz, Atomic-scale effects of chromium-doping on defect behaviour in uranium dioxide fuel, J. Nucl. Mater. 488 (2017) 160—172.

[51] S.T. Murphy, M.W.D. Cooper, R.W. Grimes, Point defects and non-stoichiometry in thoria, Solid State Ionics 267 (2014) 80—87.

[52] J.-P. Crocombette, First-principles study with charge effects of the incorporation of iodine in UO_2, J. Nucl. Mater. 429 (2012) 70—77.

[53] G. Kresse, J. Hafner, Ab initio molecular dynamics for open-shell transition metals, Phys. Rev. B 48 (1993) 13115—13118.

[54] G. Kresse, J. Furthmüller, Efficient iterative schemes for ab initio total-energy calculations using a plane-wave basis set, Phys. Rev. B 54 (1996) 11169—11186.

[55] G. Kresse, J. Furthmüller, Efficiency of ab-initio total energy calculations for metals and semiconductors using a plane-wave basis set, Comput. Mater. Sci. 6 (1996) 15—50.

[56] A.I. Lichtenstein, V.I. Anisimov, J. Zaanen, Density-functional theory and strong interactions: orbital ordering in mott-hubbard insulators, Phys. Rev. B 52 (1995) R5467.

[57] P.E. Blöchl, Projector augmented-wave method, Phys. Rev. B 50 (1994) 17953—17979.

[58] G. Kresse, D. Joubert, From ultrasoft pseudopotentials to the projector augmented-wave method, Phys. Rev. B 59 (1999) 1758—1775.

[59] S.L. Dudarev, D.N. Mahn, A.P. Sutton, Effect of mott-hubbard correlations on the electronic structure and structural stability of uranium dioxide, Philos. Mag. A B 75 (1997) 613.

[60] D.A. Andersson, P. Garcia, X.-Y. Liu, G. Pastore, M. Tonks, P. Millett, B. Dorado, D.R. Gaston, D. Andrs, R.L. Williamson, R.C. Martineau, B.P. Uberuaga, C.R. Stanek, Atomistic modeling of intrinsic and radiation-enhanced fission gas (Xe) diffusion in $UO_{2\pm x}$: implications for nuclear fuel performance modeling, J. Nucl. Mater. 451 (2014) 225—242.

[61] B. Dorado, G. Jomard, M. Freyss, M. Bertolus, Stability of oxygen point defects in UO_2 by first-principles DFT+U calculations: occupation matrix control and Jahn-teller distortion, Phys. Rev. B 82 (2010), 035114.

[62] M. Iwasawa, Y. Chen, Y. Kaneta, T. Ohnuma, H.-Y. Geng, M. Kinoshita, First-principles calculation of point defects in uranium dioxide, Mater. Trans. 47 (2006) 2651—2657.

[63] E. Vathonne, J. Wiktor, M. Freyss, G. Jomard, M. Bertolus, DFT+U investigation of charged point defects and clusters in UO_2, J. Phys. Condens. Matter 26 (2014) 349601.

[64] B. Dorado, A. Amadon, M. Freyss, M. Bertolus, DFT+U calculations of the ground state and metastable states of uranium dioxide, Phys. Rev. B 79 (2009) 235125.

[65] B. Meredig, A. Thompson, H.A. Hansen, C. Wolverton, A. Van der Walle, Method for locating low-energy solutions within DFT+U, Phys. Rev. B 82 (2010) 195128.

[66] N.J. Mosely, P. Liao, E. Carter, Rotationally invariant ab initio evaluation of Coulomb and exchange parameters for DFT+U calculations, J. Chem. Phys. 129 (2008), 014103.

[67] L. Wang, T. Maxisch, G. Ceder, Oxidation energies of transition metal oxides within the GGA+U framework, Phys. Rev. B 73 (2006) 195107.

[68] C. Franchini, R. Podloucky, J. Paier, M. Marsman, G. Kresse, Ground-state properties of multivalent manganese oxides: density functional and hybrid density functional calculations, Phys. Rev. B 75 (2007) 195128.

[69] G. Rollmann, A. Rohrbach, P. Entel, J. Hafner, First-principles calculation of the structure and magnetic phases of hematite, Phys. Rev. B 69 (2004) 165107.

[70] R.-P. Blum, H. Niehus, C. Hucho, R. Fortrie, M.V. Ganduglia-Pirovano, J. Sauer, S. Shaikhutdinov, H.-J. Freund, Surface metal-insulator transition on a vanadium pentoxide (001) single crystal, Phys. Rev. Lett. 99 (2007) 226103.

[71] M.E. Arroyo-de Dompablo, A.M.T. Morales-Garcia, DFT+U calculations of crystal lattice, electronic structure, and phase stability under pressure of TiO_2 polymorphs, J. Chem. Phys. 135 (2011), 054503.

[72] P. Santini, R. Lemánski, P. Erdos, Magnetism of actinide compounds, Adv. Phys. 48 (1999) 537—653.

[73] B. Dorado, P. Garcia, First-principles DFT+U modeling of actinide-based alloys: application to paramagnetic phases of UO2 and (U,Pu) mixed oxides, Phys. Rev. B 87 (2013) 195139.

[74] H.J. Monkhorst, J.D. Pack, Special points for brillouin-zone integrations, Phys. Rev. B 13 (1976) 5188—5192.

[75] M. Leslie, N.J. Gillan, The energy and elastic dipole tensor of defects in ionic crystals calculated by the supercell method, J. Phys. C Solid State Phys. 18

[76] S. Lany, A. Zunger, Accurate prediction of defect properties in density functional supercell calculations, Model. Simulat. Mater. Sci. Eng. 17 (2009), 084002.

[77] S.E. Taylor, F. Bruneval, Understanding and correcting the spurious interactions in charged supercells, Phys. Rev. B 84 (2011), 075155.

[78] J.-P. Crocombette, F. Jollet, L. Thien Nga, T. Petit, Plane-wave pseudopotential study of point defects in uranium dioxide, Phys. Rev. B 64 (2001), 104107.

[79] J.D. Gale, GULP: a computer Program for the symmetry-adapted simulation of solids, J. Chem. Soc., Faraday Trans. 93 (1997) 629—637.

[80] G. Busker, A. Chroneos, R.W. Grimes, I.-W. Chen, Solution mechanisms for dopant oxides in yttria, J. Am. Ceram. Soc. 82 (1999) 1553—1559.

[81] J.K. Fink, Thermophysical properties of uranium dioxide, J. Nucl. Mater. 279 (2000) 1—18.

[84] M.W. Finnis, A.Y. Lozovoi, A. Alavi, THE OXIDATION OF NIAL: what can we learn from ab initio calculations? Annu. Rev. Mater. Res. 35 (2005) 167.

[85] S.S. Zumdal, Chemical Principles, sixth ed., Houghton Mifflin Company, 2009.

[86] S.T. Murphy, D.M. Hine, Point defects and non-stoichiometry in Li_2TiO_3, Chem. Mater. 26 (2014) 1629—1638.

[87] C.E. Rice, W.R. Robinson, Structural changes in the solid solution $(Ti_{1-x}V_x)_2O_3$ as varies from zero to one, J. Solid State Chem. 21 (1977) 145—154.

[88] C.E. Rice, W.R. Robinson, High-temperature crystal chemistry of Ti_2O_3: structural changes accompanying the semiconductor-metal transition, Acta Crystallogr. B 33 (1977) 1342—1348.

[89] H. Sawada, Residual electron density study of chromium sesquioxide by crystal structure and scattering factor refinement", Mater. Res. Bull. 29 (1994) 239—245.

[90] L.W. Finger, R.M. Hazen, Crystal structure and compression of ruby to 46 kbar, J. Appl. Phys. 49 (1978) 5823—5826.

[91] S. Geller, Structure of α-Mn_2O_3, $(Mn_{0.983}Fe_{0.017})_2O_3$ and $(Mn_{0.37}Fe0.63)_2O_3$ and relation to magnetic ordering, Acta Crystallogr. B 27 (1971) 821—828.

[92] M.E. Fleet, The structure of magnetite, Acta Crystallogr. B 37 (1981) 917—920.

[93] M. Ghedira, H. Vincent, M. Marezio, J.C. Launay, Structural aspects of the metal-insulator transitions in $V_{0.985}Al_{0.015}O_2$, J. Solid State Chem. 22 (1977) 423—438.

[94] S. Asbrink, The crystal structure of and valency distribution in the low-temperature modification of V_3O_5. The decisive importance of a few very weak reflexions in a crystal-structure determination, Acta Crystallogr. B 36 (1980) 1332—1339.

[95] N. Bahlawane, D. Lenoble, Vanadium oxide compounds: structure, properties, and growth from the gas phase, Chem. Vap. Depos. 20 (2014) 299—311.

[96] W.H. Baur, A.A. Khan, Rutile-type compounds. IV. SiO_2, GeO_2 and a comparison with other rutile-type structures, Acta Crystallogr. B 27 (1971) 2133—2139.

[97] A. Yamamoto, Modulated structure of wustite $(Fe_{1-x}O)$ (three-dimensional modulation), Acta Crystallogr. B 38 (1982) 1451—1456.

[98] S. Sasaki, K. Fujino, Y. Takeuchi, X-ray determination of electron-density distributions in oxides, MgO, MnO, CoO, and NiO, and atomic scattering factors of their constituent atoms, Proc. Jpn. Acad. 55 (1979) 43—48.

[99] D.A. Andersson, P.A. Korzhavyi, Thermodynamics of structural vacancies in titanium monoxide from first-principles calculations, Phys. Rev. B 71 (2005) 144101.

[100] M.W.D. Cooper, D.A. Andersson, C.R. Stanek, US Provisional Patent Application 2017, Serial No. 62/544,673.

[101] E.O. Hall, The deformation and ageing of mild steel: III discussion of results, Proc. Phys. Soc., London 64 (1951) 747—753.

[102] N.J. Petch, The cleavage strength of polycrystals, J. Iron Steel Inst. London 173 (1953) 25—28.

[103] C.R.A. Catlow, Fission gas diffusion in uranium dioxide, Proc. R. Soc. A 364 (1978) 473—497.

[104] R.G.J. Ball, R. Grimes, A comparison of the behaviour of fission gases in $UO_{2\pm x}$ and α-U_3O_{8-z}, J. Nucl. Mater. 188 (1992) 216—221.

[105] D.A. Andersson, B.P. Uberuaga, P.V. Nerikar, C. Unal, C.R. Stanek, U and Xe transport in $UO_{2\pm x}$: density functional theory calculations, Phys. Rev. B 84 (2011), 054105.

[106] S. Beschnitt, T. Zacherle, R.A. De Souza, Computational study of cation diffusion in ceria, J. Phys. Chem. C 119 (2015) 27307—27315.

[107] P.-L. Chen, I.-W. Chen, Grain growth in CeO_2: dopant effects, defect mechanism, and solute drag, J. Am. Ceram. Soc. 77 (1994) 2289—2297.

[108] P.-P. Dholabhai, J.-A. Aguiar, L. Wu, T.G. Holesinger, T. Aoki, R.H.R. Castro, B.P. Uberuaga, Structure and segregation of dopant-defect complexes at grain boundaries in nanocrystalline doped ceria, Phys. Chem. Chem. Phys. 17 (2015) 15375.

[109] K. Gesi, J. Tateno, Dielectric constant of UO_2 at 9.4 GHz, J. Appl. Phys. 8 (1969) 1358—1359.